A new SPECT reconstruction algorithm based on the Novikov's explicit inversion formula

L.Kunyansky
California Institute of Technology
Pasadena, CA 91125

Abstract

We present a new reconstruction algorithm for the single-photon emission computed tomography (SPECT). The algorithm is based on the Novikov's explicit inversion formula for the attenuated Radon transform with non-uniform attenuation. Our reconstruction technique can be viewed as a generalization of both the filtered backprojection algorithm and the Tretiak-Metz algorithm. We test performance of the present algorithm in a variety of numerical experiments. Our numerical examples show that the algorithm is capable of accurate image reconstruction even in the case of strongly non-uniform attenuation coefficient, similar to the one occurring in a human thorax.

1 Introduction

Single-photon emission computed tomography (SPECT) is based on measurements of gamma-rays radiated by trace amounts of a radionuclide injected into a patient. The intensities of the radiation measured by a spatially collimated gamma-camera are related to values of line integrals of the radionuclide distribution, with exponential weights representing attenuation of radiation on its way from a source to the detector. The sought quantity is the radionuclide distribution; it has to be reconstructed numerically from the measured data. The above-mentioned exponential weights are determined by a position-dependent attenuation coefficient; when SPECT is performed in such regions as human thorax, this dependence cannot be neglected and has to be accounted for by the reconstruction algorithm. In this paper we present a new numerical technique, which, being based on the explicit formula recently discovered by R. Novikov [1], allows for accurate non-iterative SPECT reconstruction in presence of arbitrary realistic attenuation.

The variety of the existing SPECT algorithms can be split into a family of analytical methods [3]-[9] and a wide class of iterative techniques (see, for example [13]-[19]). Some of iterative algorithms (such as, for instance,[21]-[24]) involve evaluation of certain analytic inversion formulas as a part of the method. The advantage of the iterative techniques lies in their flexibility, which allows one to treat realistic mathematical models of the measurements, and, therefore, not only to account for the attenuation of radiation but also to correct for such image degradation factors as collimator blurring and photon scattering. The analytic methods in general, on the other hand, are considerably faster; a wide use of the filtered backprojection algorithm (FBP) in practical X-ray tomography is explained by the efficiency of this analytic technique (see [20] for the description of the FBP algorithm). However, to design an analytic method one needs an explicit inversion formula, which, for realistic mathematical models of the measurements can be difficult to derive — as it is in the case of the SPECT.

First analytic methods for the attenuation correction in SPECT were proposed two decades ago by Bellini *et al* [3] and Tretiak and Metz [4]; both algorithms assumed that the attenuation coefficient was constant inside a patient's body and that the cross-section of the body was convex. Two more analytic methods have been introduced almost a decade later in [5] and [6] (an algorithm similar to [5] was independently developed in [7], [8]). A scheme generalizing all of the above-mentioned approaches has been proposed in [9]; a general analytic approach leading to a variety of reconstruction formulas was given in [10]. Certain extensions to the underlying assumptions of constant attenuation and convex body were treated in [10] and [11]; in the former work an inversion formula was derived for the case when attenuation depends on an observation angle (but is constant for a fixed angle). All of these analytic methods, however, are not applicable for the SPECT of regions with strongly non-uniform attenuation. Creation of the analytic SPECT reconstruction algorithm operative in the case of arbitrary realistic attenuation coefficient, has become possible only recently, due to the approach developed in [12], and due to the discovery of an explicit inversion formula for the attenuated Radon transform by R. Novikov [1]. (A simpler derivation of a similar formula was given later by F. Natterer [2]).

Thus, in this paper we present a new reconstruction algorithm based on the Novikov's explicit inversion formula. Since, as we will show, the Novikov's formula can be viewed as a generalization of both the Radon inversion formula and the Tretiak-Metz formula, the resulting method contains both the FBP and the Tretiak-Metz scheme (in the cases of zero and constant attenuation, respectively). We test our algorithm using realistic models of attenuation and several activity distribution models. As our numerical experiments show, the use of the explicit inversion scheme allows for accurate non-iterative image reconstruction even within the regions with strongly non-uniform attenuation distributions, similar to the attenuation within a human thorax. In order to further reduce sensitivity of the algorithm to noise and insufficient sampling of data, in Section 6 we propose certain regularization techniques. As presented in Section 7, test reconstructions performed from both accurate and noisy data show that these regularization techniques reduce the noise sensitivity of our method to the level of noise sensitivity of the FBP algorithm. The reconstruction technique we present can be used either directly or as an efficient pre-conditioner for more complicated reconstruction algorithms capable of correcting not only for effects of non-uniform attenuation but also for other image degradation factors, such as detector blurring and/or photon scattering.

2 Formulation of the problem

Let $f(\mathbf{x})$ denote the object radionuclide distribution and $a(\mathbf{x})$ be the attenuation coefficient of the body tissue. As shown in Figure 1, the detector measures intensity of radiation $g_\varphi(p)$ emitted in the direction $\theta(\varphi)$ along a line defined by its distance p from the origin; the values of $g_\varphi(p)$ are given by the following equation:

$$g_\varphi(p) \equiv R_{a,\varphi} f = \int_{\mathbb{R}} \exp\left(-D_\varphi a[\mathbf{x} + t\theta(\varphi)]\right) f(\mathbf{x} + t\theta(\varphi)) dt, \tag{1}$$

where the divergent beam transform $D_\varphi a(\mathbf{x})$ is defined as follows

$$D_\varphi a(\mathbf{x}) = \int_0^\infty a(\mathbf{x} + t\theta(\varphi)) dt. \tag{2}$$

The integral transform given by Equation (1) maps function $f(\mathbf{x})$ into its projections $g_\varphi(p)$; this transform is usually referred to as the attenuated Radon transform. We will assume that the

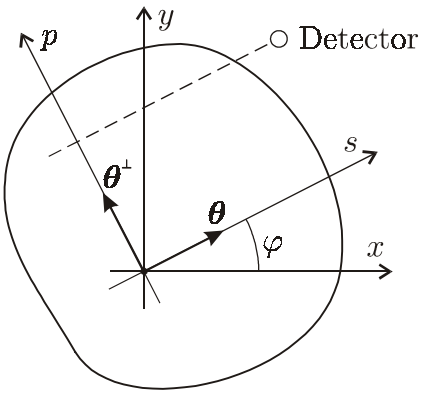

Figure 1: Data acquisition scheme and coordinate systems

attenuation coefficient is known (in practice it can be obtained, for example, from transmission measurements as it is done in [25] and [26]). The goal of SPECT is to reconstruct the radionuclide distribution $f(\mathbf{x})$ from measured projections $g_\varphi(p)$. The reconstruction algorithm we present is based on the Novikov's explicit inversion formula for the attenuated Radon transform.

3 Novikov's explicit inversion formula

In order to simplify presentation we introduce a rotated coordinate system (s,p) with axes parallel to vectors $\theta(\varphi)$ and $\theta^\perp(\varphi)$ (see Figure 1) so that

$$\begin{aligned} s &= x\cos\varphi + y\sin\varphi, \\ p &= -x\sin\varphi + y\cos\varphi. \end{aligned}$$

In the new coordinates the integrations defined by Equations (1, 2) can be written in a particularly simple form:

$$g_\varphi(p) \equiv \int_{\mathbb{R}} \exp\left(-D^*_\varphi a^*_\varphi(s,p)\right) f^*_\varphi(s,p)ds, \tag{3}$$

$$D^*_\varphi a^*_\varphi(s,p) = \int_s^\infty a^*_\varphi(s',p)ds', \tag{4}$$

where $f^*_\varphi(s,p) = f(\mathbf{x}(s,p,\varphi))$, $a^*_\varphi(s,p) = a(\mathbf{x}(s,p,\varphi))$, and $D^*_\varphi a^*_\varphi(s,p) = D_\varphi a(\mathbf{x}(s,p,\varphi))$.

The (classical) Radon transform R_φ of the attenuation coefficient $a(\mathbf{x})$ is defined by the following equation

$$R_\varphi a(p) = \int_{-\infty}^\infty a^*_\varphi(s',p)ds'. \tag{5}$$

Comparing this expression to (4) one observes that the values of $R_\varphi a(p)$ coincide with limiting values of the divergent beam transform D_φ :

$$R_\varphi a(p) = D^*_\varphi a^*_\varphi(-\infty,p).$$

The goal of the SPECT reconstruction is to recover the radionuclide distribution $f(\mathbf{x})$ from projections $g_\varphi(p)$. This problem is equivalent to the inversion of the attenuated Radon transform (1), under assumption that the attenuation coefficient $a(\mathbf{x})$ is known. The explicit inversion formula for this transform has been derived recently by R. Novikov [1]. We present the Novikov's formula below in a slightly simplified equivalent version that avoids usage of complex-valued integral transforms:

$$f(\mathbf{x}) = \frac{1}{4\pi}\left(\frac{\partial}{\partial x_2}B^c(\mathbf{x}) - \frac{\partial}{\partial x_1}B^s(\mathbf{x})\right), \tag{6}$$

$$\begin{aligned} B^c(\mathbf{x}) &= \int_0^{2\pi} \exp(D_\varphi a(\mathbf{x}))m_\varphi(\mathbf{x}\cdot\theta^\perp(\varphi))\cos\varphi d\varphi, \\ B^s(\mathbf{x}) &= \int_0^{2\pi} \exp(D_\varphi a(\mathbf{x}))m_\varphi(\mathbf{x}\cdot\theta^\perp(\varphi))\sin\varphi d\varphi, \end{aligned} \tag{7}$$

where the modified projections $m_\varphi(p)$ are defined as

$$m_\varphi(p) = e^{-A_\varphi(p)}\left[h^c_\varphi(p)H\left(h^c_\varphi(p)e^{A_\varphi(p)}g_\varphi(p)\right) + h^s_\varphi(p)H\left(h^s_\varphi(p)e^{A_\varphi(p)}g_\varphi(p)\right)\right], \tag{8}$$

the Hilbert transform H of a function $\psi(u)$ is given by the formula

$$H\psi(u) = \frac{1}{\pi}\mathcal{P}\int_{\mathbb{R}}\frac{\psi(v)}{u-v}dv, \tag{9}$$

and

$$\begin{aligned} h^c_\varphi(p) &= \cos(HA_\varphi(p)), \\ h^s_\varphi(p) &= \sin(HA_\varphi(p)), \\ A_\varphi(p) &= \frac{1}{2}\left(R_\varphi a\right)(p). \end{aligned} \tag{10}$$

One can further modify the Novikov's formula to a form similar to the Radon or Tretiak-Metz inversion formulas. Namely, note that the differential operator $(-\sin\varphi\frac{\partial}{\partial x_1}, \cos\varphi\frac{\partial}{\partial x_2})$ is equal to $(\theta^\perp(\varphi)\cdot\nabla)$. Application of this operator to a function in (s,p) coordinates is equivalent to differentiation in p, so that formulas (6, 7) can be replaced by the formulas

$$f(\mathbf{x}) = \frac{1}{4\pi}\int_0^{2\pi} M_\varphi(\mathbf{x}\cdot\theta(\varphi), \mathbf{x}\cdot\theta^\perp(\varphi))d\varphi, \tag{11}$$

$$M_\varphi(s,p) = \frac{\partial}{\partial p}\left[\exp(D^*_\varphi a^*_\varphi(s,p))m_\varphi(p)\right]. \tag{12}$$

4 Relation between the Novikov's and Tretiak-Metz inversion formulas

Analyzing Equations (11, 12) one can easily notice that in the case when attenuation is absent (i.e. $a(\mathbf{x}) = 0$) the Novikov's inversion formula can be reduced to one of the known inversion formulas for the classical Radon transform (namely, to the formula that involves differentiation and the Hilbert transform of the projections followed by the backprojection step (see [20])).

In this section we will show that the Novikov's formula also contains the known Tretiak-Metz inversion formula [4] as a particular case.

The formula proposed by Tretiak and Metz allows one to invert the attenuated Radon transform (1) in the case when the body has a convex cross-section and the attenuation coefficient $a(\mathbf{x})$ is equal to some constant μ inside this cross-section. Throughout this section we will assume that these two conditions hold.

Notice first, that, under assumptions we have made, the reconstruction problem can be reformulated into a similar problem with the attenuation $a(\mathbf{x}) = \mu$ supported inside a disk; we will assume, without loss of generality, that the radius of the disk is equal to unity. Then, according to Tretiak-Metz inversion scheme, activity $f(\mathbf{x})$ can be reconstructed as a result of the following sequence of operations:

1. Pre-multiplication of projections $g_\varphi(p)$, $p \in [-1, 1]$ by the factor $e^{\mu\sqrt{1-p^2}}$;
2. Filtration of the pre-multiplied projections with the filter $w(p)$ given by the following formulas

$$\hat{w}(\rho) = \begin{cases} 0 & , \quad |\rho| < \mu \\ |\rho| & , \quad |\rho| \geq \mu \end{cases}, \quad \hat{w}(\rho) = (Fw)(\rho) \tag{13}$$

   where the Fourier transform F of a function $u(p)$ is defined as

$$\hat{u}(\rho) = Fu = (2\pi)^{-1/2} \int_{\mathbb{R}^1} e^{-i\rho p} u(p) dp; \tag{14}$$

3. Backprojection with the weight $e^{-\mu(\mathbf{x}\cdot\theta(\varphi))}$ of the filtered projections $G_\varphi(p)$ obtained on the previous step:

$$f(\mathbf{x}) = \frac{1}{4\pi} \int_0^{2\pi} e^{-\mu(\mathbf{x}\cdot\theta(\varphi))} G_\varphi(\mathbf{x}\cdot\theta^\perp(\varphi)) d\varphi.$$

One can readily verify that the factor $e^{A_\varphi(p)}$ in Equation (8) under assumptions of this section coincides with the function $e^{\mu\sqrt{1-p^2}}$ utilized on the first step of the Tretiak-Metz scheme. It is also easy to see that the combination of the factors $e^{-A_\varphi(p)}$ from Equation (8) and $\exp(D^*_\varphi a^*_\varphi(s,p))$ from Equation (12) does not depend on p, so that (12) can be re-written as

$$f(\mathbf{x}) = \frac{1}{4\pi} \int_0^{2\pi} e^{-\mu(\mathbf{x}\cdot\theta(\varphi))} \left(\frac{\partial}{\partial p} m_\varphi\right)(\mathbf{x}\cdot\theta^\perp(\varphi)) d\varphi.$$

In other words, the last step of the Novikov's inversion scheme coincides with the last step of the Tretiak-Metz method.

In order to prove the equivalence of the two inversion formulas under assumptions of this section, one has to show that the Novikov's filtration operator Nu defined according to Equations (8, 12) by the formulas

$$Nu(p) = \frac{\partial}{\partial p} \Upsilon u(p), \tag{15}$$

$$\Upsilon u(p) = h^c_\varphi(p) H\left(h^c_\varphi(p) u(p)\right) + h^s_\varphi(p) H\left(h^s_\varphi(p) u(p)\right), \tag{16}$$

with functions $h^c_\varphi(p)$ and $h^s_\varphi(p)$ given by (10), is equivalent to the filtration with the filter $w(p)$ (see Equation (13)) used in the Tretiak-Metz scheme. Let us notice first that the function $A_\varphi(p)$

and its Hilbert transform $HA_\varphi(p)$ in Equation (10) under our assumptions can be evaluated for values of p in the interval $[-1,1]$ as follows

$$A_\varphi(p) = \begin{cases} \mu\sqrt{1-p^2} & , \quad |p| \le 1 \\ 0 & , \quad |p| > 1 \end{cases} , \tag{17}$$

$$HA_\varphi(p) = \mu p; \tag{18}$$

for the proof of (18) see Appendix. Now the operator $\Upsilon u(p)$ can be represented as follows:

$$\begin{aligned} \Upsilon u(p) &= \cos(\mu p) H\left(\cos(\mu p) u(p)\right) + \sin(\mu p) H\left(\sin(\mu p) u(p)\right) \\ &= \frac{1}{2}\left[e^{i\mu p} H(e^{-i\mu p} u(p)) + e^{-i\mu p} H(e^{i\mu p} u(p))\right]. \end{aligned}$$

Taking into account that multiplication by the factor $e^{i\mu p}$ shifts the Fourier transform $\hat{u}(\rho)$ of the function $u(p)$ by μ, and that the Hilbert transform H multiplies $\hat{u}(\rho)$ by $(-i \operatorname{sign} \rho)$, one sees that the Fourier transformant $\widehat{\Upsilon u}(\rho)$ of the function $\Upsilon u(p)$ is given by

$$\widehat{\Upsilon u}(\rho) = -i(\hat{u}^+(\rho) - \hat{u}^-(\rho)), \tag{19}$$

where

$$\hat{u}^+(\rho) = \begin{cases} \hat{u}(\rho) & , \quad \rho \ge \mu \\ 0 & , \quad \rho < \mu \end{cases} , \quad \hat{u}^-(\rho) = \begin{cases} \hat{u}(\rho) & , \quad \rho \le -\mu \\ 0 & , \quad \rho > -\mu \end{cases} . \tag{20}$$

Equation (19) allows one to evaluate the Fourier transform $\widehat{Nu}(\rho)$ of $Nu(p)$; namely, since differentiation $\partial/\partial p$ is equivalent to multiplication of the Fourier transform of a function by the factor $i\rho$, the transformant $\widehat{Nu}(\rho)$ is given by the following expression

$$\widehat{Nu}(\rho) = |\rho|\left(\hat{u}^+(\rho) + \hat{u}^-(\rho)\right).$$

Comparing the above equation with the expression for the Tretiak-Metz's filter (13) we see that, under assumptions of this section, the two formulas are equivalent, i.e. they represent the same left inverse operator.

5 Reconstruction algorithm

According to Equations (8)-(12) one can reconstruct radionuclide distribution $f(\mathbf{x})$ from the projections $g_\varphi(p)$ by:

1. Evaluating the divergent beam transform $D_\varphi a(\mathbf{x})$ and the Radon transform $R_\varphi a(p)$;
2. Evaluating the Hilbert transformant of $A_\varphi(p)$;
3. Computing modifying projections $m_\varphi(p)$ (see Equation (8));
4. Differentiating the product $\exp(D^*_\varphi a^*_\varphi(s,p)) m_\varphi(p)$ in p, (see Equation (12));
5. Backprojecting the result of the differentiation $M_\varphi(s,p)$ (see Equation 11).

The reconstruction algorithm we present follows the structure of the inversion formula. We assume that the data $g_\varphi(p)$ are discretized uniformly in both radial (p) and angular (φ) variables, i.e. values of $g_{\varphi_i}(p_j), i = 1, 2, ...n^\varphi, j = 1, 2, ...n^p$ are given, where n^φ is the number of projections, n^p is the discretization size of each projection, $\varphi_i = 2\pi(i-1)/n^\varphi$, $p_j = -R + \Delta p(j-1), \Delta p = 2R/(n^p - 1)$, and where R is the radius of the image support. It is also assumed that the attenuation coefficient $a(\mathbf{x})$ is known and given by its values on the same Cartesian grid on which the image will be reconstructed.

The discretization of the projections suggests natural discretization for most of the involved functions and integral transforms. In particular, we will approximate backprojection (11) by the following finite sum:

$$f(\mathbf{x}) \approx \frac{2\pi}{n^\varphi} \sum_{i=1}^{n^\varphi} M_{\varphi_i}(\mathbf{x} \cdot \theta(\varphi_i), \mathbf{x} \cdot \theta^\perp(\varphi_i)), \quad i = 1, 2, ...n^\varphi. \tag{21}$$

Accordingly, we will have to compute values of all other quantities used in the algorithm corresponding to the values $\varphi_i, i = 1, 2, ...n^\varphi$.

5.1 Divergent beam transform

For each given angle φ_i we evaluate the divergent beam transform $D^*_\varphi a^*_\varphi(s, p)$ using integration in (s, p) coordinate system, as given by Equation (4), for each value of $p_j, j = 1, 2, ...n^p$. The integrals are computed using the trapezoidal rule with the step $\Delta s = \Delta p$. Since the object's cross-section has a finite support the integration domain is finite (i.e., $[s, \sqrt{R^2 - p^2}]$. Moreover, use of the trapezoidal rule leads to the following recurrence relation:

$$\begin{aligned} D^*_\varphi a^*_\varphi(-R + k\Delta s, p) \;\approx\; & D^*_\varphi a^*_\varphi(-R + (k+1)\Delta s, p) \\ & + \frac{\Delta s}{2}[a^*_\varphi(-R + k\Delta s, p) + a^*_\varphi(-R + (k+1)\Delta s, p)]. \end{aligned}$$

This recurrence relation allows us to obtain $(n^p)^2$ values $D^*_{\varphi_i} a^*_{\varphi_i}(s_k, p_j), \quad j, k = 1, 2, ...n^p$ on the (s, p) grid in $\mathcal{O}((n^p)^2)$ operations, where $s_k = -R + \Delta s(k-1)$. Since the values of the attenuation coefficient $a(\mathbf{x})$ are given at the nodes of the Cartesian grid in (x, y) coordinates, the bilinear interpolation is used to obtain values of $a^*_\varphi(s, p) = a(\mathbf{x}(s, p, \varphi))$ necessary for the integration in (s, p) coordinates.

Due to the Equation (5), after the divergent transform is computed for the current value of φ_i, we automatically obtain values of $A_{\varphi_i}(p_j)$, $j = 1, 2, ...n^p$ (see Equation (10)); they are equal simply to $D^*_{\varphi_i} a^*_{\varphi_i}(s_1, p_j)$.

5.2 Hilbert transform

Having computed $A_{\varphi_i}(p_j)$, $j = 1, 2, ...n^p$ for a given angle φ_i, one can evaluate the Hilbert transform of $A_{\varphi_i}(p)$ as required by (10). The Hilbert transform can be viewed as a convolution with the kernel $1/(\pi p)$; we approximate such a convolution by a discrete convolution with the regularized kernel represented by the following sequence of values K_j, $j = -n_p, ..., n_p$:

$$\begin{aligned} K_j &= \frac{1}{\pi}\left[j \ln(1 - \frac{1}{j^2}) + \ln\frac{j+1}{j-1}\right], \quad j = 2, ..., n_p \\ K_1 &= \frac{2}{\pi}\ln 2, \quad K_0 = 0, \\ K_{-j} &= -K_j, \quad j = -n_p, ..., 1. \end{aligned}$$

This sequence can be viewed as values of the regularized kernel $1/(\pi p) * \eta(p)$ at the points $p = p_j$, where the roof-top function $\eta(p)$ is defined as

$$\eta(p) = \begin{cases} \frac{1}{\Delta p}(p+1) & , \quad -\Delta p \le p \le 0, \\ \frac{1}{\Delta p}(1-p) & , \quad 0 \le p \le \Delta p, \\ 0 & , \quad |p| > \Delta p. \end{cases}$$

The use of such a discrete kernel is equivalent to performing a linear interpolation of a function between values p_j followed by exact convolution with the kernel $1/(\pi p)$,; it also can be viewed as computation of the Hilbert transform via filtration in the frequency domain performed using the following window function $w(\rho)$:

$$w(\rho) = \frac{\sin(\pi \frac{\rho}{\rho_{nyq}})}{\pi \frac{\rho}{\rho_{nyq}}}$$

where ρ_{nyq} is the Nyquist frequency of the discretization. (The use of low-pass filter $w(\rho)$ reduces sensitivity of the whole algorithm to noise in the data)

Thus, the Hilbert transform of a function is evaluated by zero padding the function (represented by n^p samples) to $2n^p$ samples, followed by the discrete convolution with the approximate kernel $\{K_j\}$ performed the Fast Fourier Transform algorithm (FFT). The above convolution technique is used in the algorithm to compute values of the functions $h^c_{\varphi_i}(p_j)$ and $h^s_{\varphi_i}(p_j)$, and to evaluate the modified projections $m_{\varphi_i}(p_j)$, see Equation (8).

5.3 Differentiation and backprojection

The differentiation of the product $\exp(D^*_\varphi a^*_\varphi(s,p))m_\varphi(p)$, as required by Equation (12) can be easily performed using finite differences. Indeed, as a result of the previous steps of the algorithm the values of this product are known at the nodes of Cartesian grid in (s,p) variables. Various finite difference differentiation techniques can be used here; all result presented in Section 7 were obtained using the following formula [27]:

$$u^{'}(p) \approx \frac{1}{12\Delta t}\left[8(u(p+2\Delta p) - u(p-2\Delta p)) - u(p+\Delta p) - u(p-\Delta p)\right].$$

As a result of the differentiation step we obtain values of $M_{\varphi_i}(s_k, p_j)$ at the nodes of the (s,p) grid.

The final step of the algorithm consists in backprojection of the previously computed quantity $M_{\varphi_i}(s,p)$, as required by Equation (21), to reconstruct the image $f(\mathbf{x})$. On this step we utilize, again, the bilinear interpolation, in order to obtain values $M_{\varphi_i}(\mathbf{x}\cdot\theta(\varphi_i), \mathbf{x}\cdot\theta^{\perp}(\varphi_i))$ from known values $M_{\varphi_i}(s_k, p_j)$.

This completes the description of the basic version of our algorithm. In the following section we will discuss certain techniques which allow to reduce sensitivity of the algorithm to possible insufficient sampling and to noise contained in data. Assuming that the number of projections n_φ, the number of samples n_p, and the size n of the reconstruction grid are of the same order, i.e. $n_\varphi \sim n_p \sim n$, one can easily conclude that the number of operations required by the basic version of the algorithm is equal to $\mathcal{O}(n^3)$.

6 Improving stability of the algorithm

The image reconstruction in X-ray tomography is equivalent to the inversion of the classical Radon transform. This problem is known to be ill-posed, so that the result of the reconstruction

is usually sensitive to noise and/or insufficient sampling of data. The ill-posedness of the inverse problem in X-ray tomography is not too severe, however, so that such reconstruction technique as the FBP algorithm allows one to obtain high-quality images from the real data. In SPECT, on the other hand, the presence of the exponential weight in the expression for the backprojection makes the Tretiak-Metz technique significantly less stable than the FBP. The basic version of the present algorithm, which can be viewed as a generalization of the Tretiak-Metz technique, has demonstrated in our numerical experiments the same level of stability as the latter method. In order to increase stability of the present algorithm and, thus, make it more suitable for practical applications, we propose below two regularization techniques.

6.1 Generation of an extended set of projections

Two of the most important factors determining quality of tomography reconstruction are the number of projections n_φ and the number n_p of samples in a single projection. The (approximately) optimal relation between the values of these parameters in case of transmission tomography is $n_\varphi/n_p \approx \frac{\pi}{2} n_p$ (see, for example [20]). Unlike the transmission tomography, where projections are measured in the angular range $[0, \pi]$, in our case of the emission tomography measurements cover the range of angles from 0 to 2π. One may assume, therefore, that in SPECT the optimal ratio of n_φ and n_p is given by

$$n_\varphi/n_p \approx \pi.$$

In practice, however, this ratio frequently falls much below the optimal value π; indeed, sets of measured data not uncommonly have dimensions 64×64 or 128×128. It is known that insufficient number of projections leads to occurrence of star-like artifacts in the reconstructed image. Our numerical experiments show that this phenomenon is considerably more pronounced when attenuation is present. To improve the quality of the reconstruction from a suboptimal number of projections, we use trigonometric approximation of the data to replace the original set of n_φ projections by a set of $2n_\varphi$ (equally spaced in angular variable) projections. Namely, for each fixed p_j we (a) expand values $g_{\varphi_i}(p_j)$ in the Fourier series in the angular variable; (b) multiply the expansion coefficients $\hat{g}_k(p_j), k = -n_\varphi/2, .., n_\varphi/2$ by a low-pass filter of the form $[\sin(2\pi|k|/n_\varphi)/(2\pi|k|/n_\varphi)]^{1/2}$; (c) zero-pad Fourier coefficients to obtain a sequence of $2n_\varphi$ values(d) evaluate the Fourier series to obtain values $g^{gen}_{\varphi^*_l}(p_j)$ of the generated projections for a given p_j and observation angles $\varphi^*_l, l = 1, ..2n_\varphi$. Then the set of the $2n_\varphi$ newly generated projections is used as an input for our basic algorithm.

Use of this technique results in significant improvements in images reconstructed from a suboptimal number of projections and/or from noisy data. The computational cost of the method is twice the cost of the basic version of our method, since the number of projections to process is doubled. (The cost of projection generation itself ($\mathcal{O}(n^2 \ln n)$) is negligible in comparison with the rest of computations).

6.2 Reduction to the unattenuated case via multiplicative correction

An alternative way of increasing stability of the algorithm and improving the image quality consists in reducing the problem in hand to the less ill-conditioned inversion of the classical Radon transform. In the case of constant attenuation such a reduction was done in [3]; in that work the unattenuated projections were computed from the attenuated ones using certain relation between the Fourier transformants of the two sets of projections. Similar relation is not readily available in the case of arbitrary attenuation; instead we will achieve the desired reduction

by the multiplicative correction technique described below. (The technique we propose is closely related to the multiplicative correction used in [23] as a part of an iterative reconstruction algorithm).

For activity distribution $f(\mathbf{x})$ the unattenuated projections $R_{0,\varphi}f(p)$ are defined by the formula (1) with $a(\mathbf{x}) = 0$. Let us introduce a corrective coefficient $k_\varphi(p)$ defined by the following equation

$$k_\varphi(p) = \begin{cases} R_{0,\varphi}f(p)/R_{a,\varphi}f(p) & , \quad R_{a,\varphi}f(p) > 0 \\ 0 & , \quad R_{a,\varphi}f(p) = 0 \end{cases} , \tag{22}$$

so that $R_{0,\varphi}f(p) = k_\varphi(p)R_{a,\varphi}f(p)$. Obviously, since $f(\mathbf{x})$ is nonnegative, the following inequalities hold

$$1 \le k_\varphi(p) \le \exp(R_\varphi a(p)) \tag{23}$$

Values of $k_\varphi(p)$ are unknown, of course; however, given a good approximation to $f(\mathbf{x})$ one can easily compute an approximation to $k_\varphi(p)$. Thus, our strategy when dealing with noisy data is described as follows:

(A) Compute an approximate version $f^{appr}(\mathbf{x})$ of the image using the basic version of the present algorithm; enforce the condition $f^{appr}(\mathbf{x}) \ge 0$;

(B) Compute $R_{0,\varphi}f^{appr}(p)$ and $R_{a,\varphi}f^{appr}(p)$ from Equation (1);

(C) Compute $k_\varphi^{appr}(p)$ from Equation (22) enforcing conditions (23);

(D) Find approximate values of unattenuated projections $R_{0,\varphi}f(p)$ by multiplying $g_\varphi(p)$ by $k_\varphi^{appr}(p)$;

(E) Reconstruct the new image from unattenuated projections using the classical FBP algorithm (or the basic version of the present algorithm with $a(\mathbf{x})$ set to zero).

Being integral quantities, computed projections $R_{0,\varphi}f^{appr}(p)$ and $R_{a,\varphi}f^{appr}(p)$ are much less affected by noise in the data than the point values of $f^{appr}(\mathbf{x})$, which allows for accurate reconstruction of the corrective factor $k_\varphi(p)$. Therefore, the noise levels in the product $g_\varphi(p)k_\varphi^{appr}(p)$ and in the projections $g_\varphi(p)$ are of the same level. On the other hand, the FBP algorithm utilized for the image reconstruction from unattenuated projections $g_\varphi(p)k_\varphi^{appr}(p)$ is much less sensitive to the noise in the data; thus, it yields image of much better quality than the initial approximation $f^{appr}(\mathbf{x})$.

In order to estimate computational expenses of the reconstruction technique described in this section, let us notice that the values of the divergent ray transform $D_\varphi^* a_\varphi^*(s,p)$ obtained while computing $f^{appr}(\mathbf{x})$ can be re-used for the evaluation of $R_{0,\varphi}f^{appr}(p)$ and $R_{a,\varphi}f^{appr}(p)$. On the other hand, one can achieve a two-fold reduction in the number of required operations on the FBP step by combining opposite projections. Altogether, all five steps (A)-(E) of our multiplicative correction technique require, roughly, twice the number of operations needed for our basic algorithm.

7 Numerical examples

7.1 Phantoms

The goal of this section is to demonstrate ability of the present technique to reconstruct images in cases of realistic attenuation coefficients, and to test sensitivity of the algorithm to non-perfect data which contain noise and may be undersampled. To this end the following model

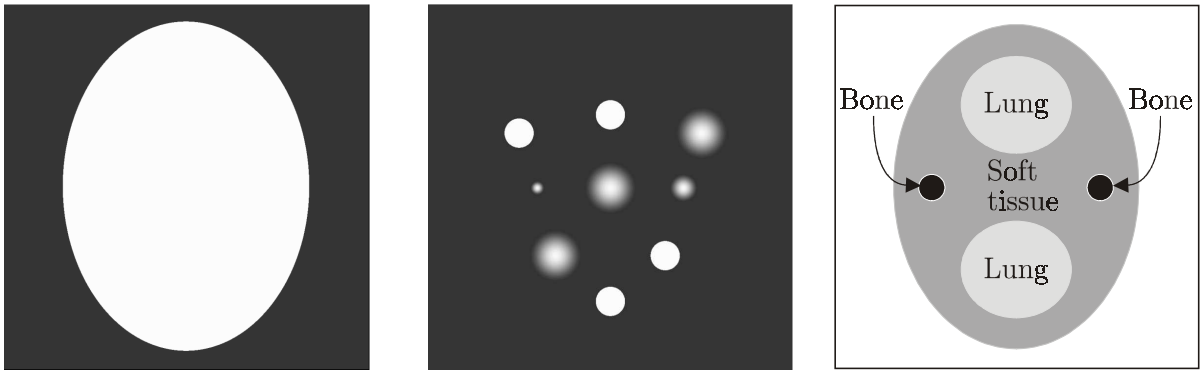

(a) (b) (c)

Figure 2: Model distributions (a) activity phantom #1 (b) activity phantom #2 (c) attenuation phantom from work [22]

radionuclide distributions will be utilized. The first activity phantom to be used is described by the characteristic function $\chi_{ell}(\mathbf{x})$ of an ellipse with the axis length ratio 3:4, see Figure 2(a). It will allow us to test the ability of the algorithm to reconstruct slowly varying spatial distributions. We will refer to this function as to the phantom #1. The second activity model we use, phantom #2, consists of a set of peak-shaped functions, see Figure 2(b). Some of these test objects are defined by characteristic functions of circles, while the others are given by functions $u_i(\mathbf{x}, \mathbf{x}_i, r_i)$ of the following form

$$u_i(\mathbf{x}, \mathbf{x}_i, r_i) = \begin{cases} (1 - (\mathbf{x} - \mathbf{x}_i)^2 / {r_i}^2) & , \quad r \leq r_i \\ 0 & , \quad r > r_i \end{cases}$$

This phantom #2 will be used to probe the ability of the algorithm to reproduce smaller details and fast varying or discontinuous distributions.

To model attenuation coefficient we use the following functions. When comparing the performance of the present algorithm to our version of the Tretiak-Metz scheme, the attenuation is modeled by the characteristic function $\chi_{ell}(\mathbf{x})$ of the ellipse (shown in Figure 2(a)) multiplied by a certain constant μ. The value of this constant is chosen so that the optical lengths of the axes are equal to 3.0375 and 4.05. (The optical length is a dimensionless quantity equal to an integral of the attenuation coefficient along a path — or, in this case, to the product of the axis length and μ).

To simulate a realistic strongly non-uniform attenuation coefficient we utilize the phantom used in work [22]. This model imitates an attenuation distribution across a section of a human thorax; it consists of an ellipsoidal body with axes of length 22.5 and $30cm$, which contains two smaller ellipsoidal regions with axes of length $10cm$ and $8.8cm$ and two circular regions

of diameter $2.5cm$, see Figure 2(c). The smaller ellipsoidal regions simulate lungs, while the circular regions correspond to bones; attenuation is equal to $0.01cm^{-1}$ within "lungs" and to $0.17cm^{-1}$ within "bones". Attenuation within the rest of the large ellipse is equal to $0.15cm^{-1}$.

The data sets for all reconstructions consist of 128 projections, each containing 129 samples; images are reconstructed on a 129×129 grid.

7.2 Reconstruction in the case of constant attenuation

In this section we test performance of the algorithm based on the Novikov's inversion formula in the case of constant attenuation. We will compare the reconstruction results to the images obtained using the author's version of the Tretiak-Metz algorithm. The filtration in our version of the Tretiak-Metz scheme is performed by computing the Fourier transform of the pre-multiplied projections using the FFT, by multiplying the transformant by the filter $\hat{w}(\rho)$ (see Equation 13), and by computing the inverse FFT.

In the first test, as model activity and attenuation distributions we use functions equal to constants inside an ellipse (see the previous section for the details). Figure 3 shows reconstruction results obtained using the basic version of the present algorithm. The reconstructed image is very close to the original in this simple case. The Tretiak-Metz algorithm also yields good results in this test.

(a) (b)

Figure 3: Reconstruction in the case of constant attenuation (a) original image (b) present algorithm.

The next set of images (Figure 4) demonstrates a series of reconstructions of the phantom #2 obtained using the Tretiak-Metz algorithm, the basic version of the present method, and the enhanced versions of our algorithm as described in Section 6. The basic version of the present method produces images of slightly better quality (Figure 4(b)) than our version of the Tretiak-Metz scheme (Figure 4(a)). The difference can be explained by a different filtration technique used in the realizations of these two very similar algorithms. By utilizing the projection generation technique or by reducing the problem to the unattenuated case one can prevent the high frequency star-like artifacts from occurring in the image, as shown in Figures 4(c), (d).

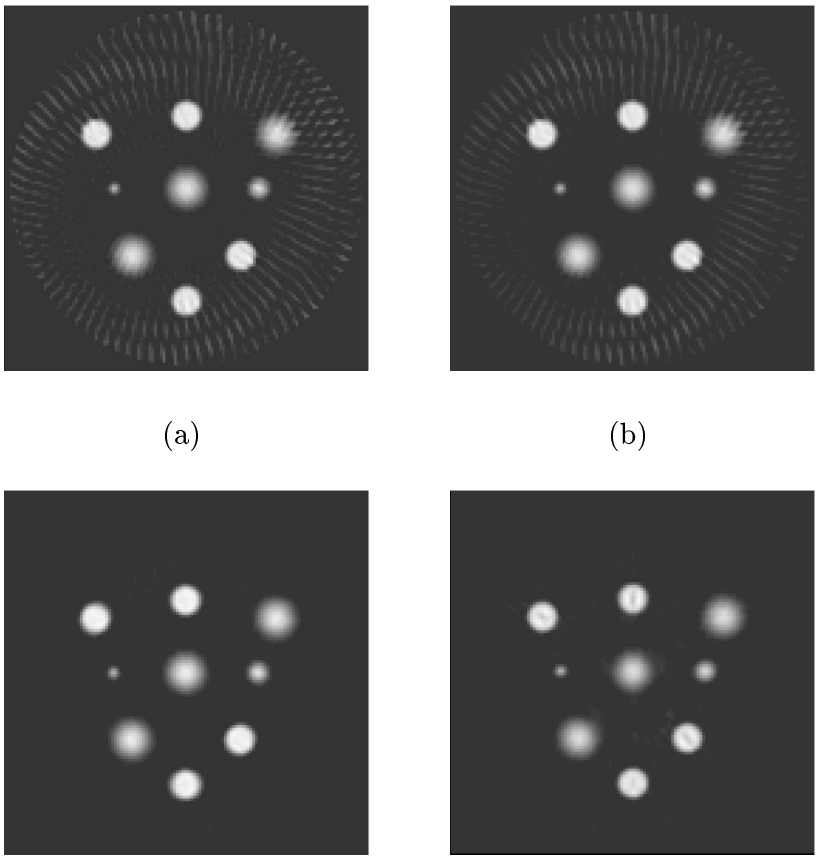

(a) (b)

(c) (d)

Figure 4: Reconstruction in the case of constant attenuation, phantom #2 (a) Tretiak-Metz algorithm (b) present basic algorithm (c) present algorithm with generation of additional projections (d) present algorithm with multiplicative correction.

7.3 Reconstruction in the case of non-uniform attenuation

This section presents results obtained in the case of strongly non-uniform attenuation coefficient as modeled by the phantom utilized in work [22] (see Figure 2(c) and the description given in Section 7.1). We experimented with both phantom #1 and phantom #2; the results are shown in Figures 5 and 6 respectively.

Figure 5(a) demonstrates the image obtained without any attenuation correction, i.e. using the (regular) FBP algorithm. Figures 5(b)-(d) show images computed by the present algorithm; the projection generation technique and the multiplicative correction (Section 6) were utilized to enhance the quality of the image shown in Figures 5(c), (d), respectively. Comparing the images (c) and (d) in Figure 5 against the image (b) one can notice a considerable decrease in the magnitude of artifacts delivered by the proposed reconstruction enhancement techniques (see also Figures 5(e) and (d) for the comparison of the cross-sections of images (c) and (d) agains image (b) along the line $x_2 = -0.5$).

Figure 6 presents the reconstruction results for the activity phantom #2. The image obtained without any attenuation correction is shown in Figure 6(a); Figures 6(b)-(d) present the images reconstructed using the present algorithm — with and without use of the image enhancement techniques. Once again, comparing the images (c) and (d) versus image (b) in Figure 6, one can notice significant improvements in image quality delivered by the projection generation technique and by the method of multiplicative correction. Figure 6(e),(f) compare the cross-sections of the images (b) and (c).

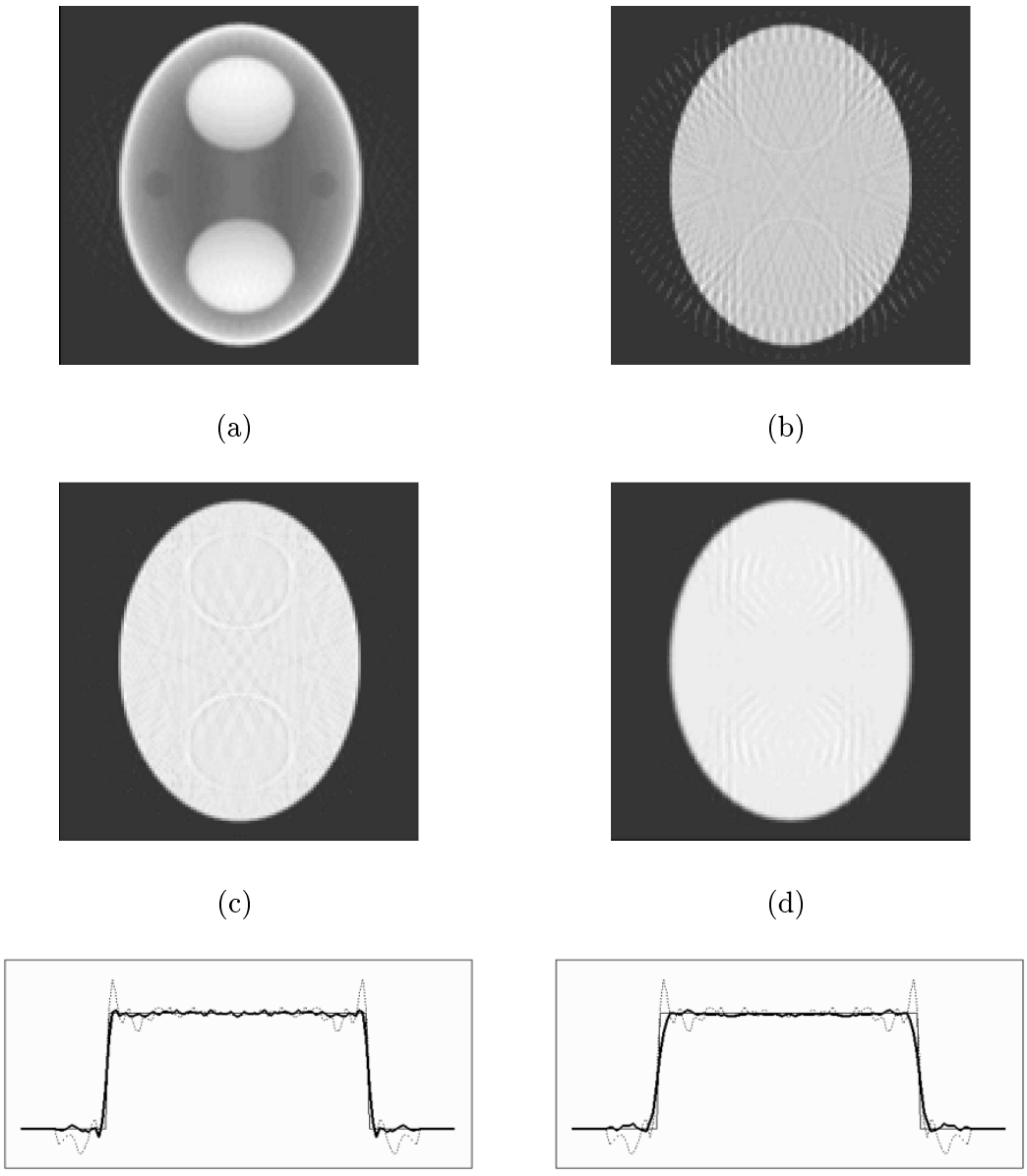

Figure 5: Reconstruction in the case of strongly non-uniform attenuation, phantom #1 (a) reconstruction with no attenuation correction (b) present algorithm (c) present algorithm with projection generation (d) present algorithm with multiplicative correction (e) comparison of images 5(b) and 5(c) (f) comparison of images 5(b) and 5(d)

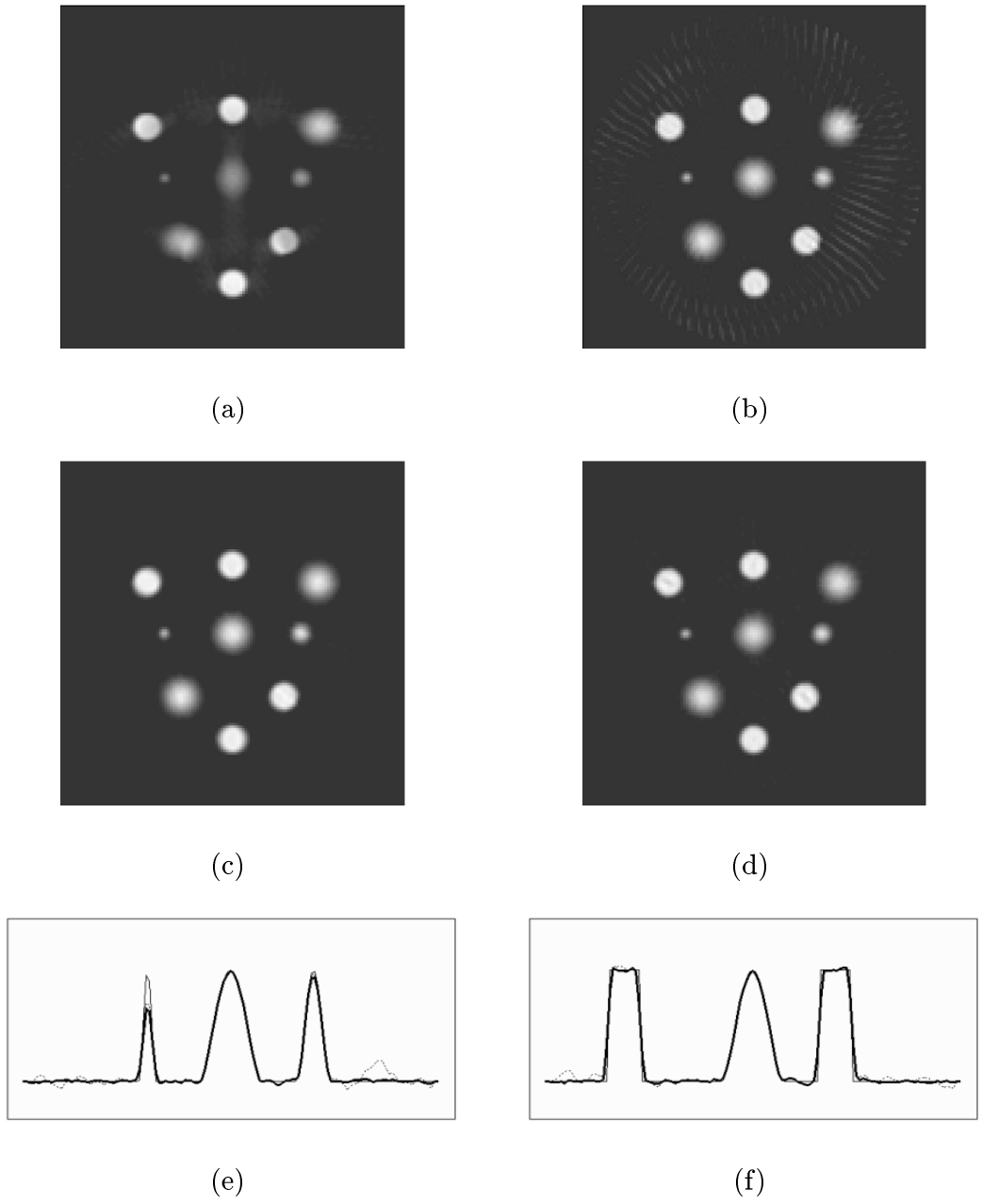

Figure 6: Reconstruction in the case of strongly non-uniform attenuation, phantom #2 (a) reconstruction with no attenuation correction (b) present algorithm (c) present algorithm with projection generation (d) present algorithm with multiplicative correction (e), (f) comparison of the image (c) against image (b): Figure (e) shows the cross-section along the line $x_2 = 0$, (f) demonstrates the cross-section along the line $x_1 = 0$; dashed line in Figures (e),(f) corresponds to the cross-sections of (b), thick line represents (c), and the exact result is shown by the thin solid line.

7.4 Reconstruction from noisy data

In this section we present results of the reconstruction from noisy data. The same model functions are used as in the previous section; in order to simulate quantum noise in the data the model projections are multiplied by a factor $(1 + c\mathcal{S}_\varphi(p))$, where $\mathcal{S}_\varphi(p)$ is a random variable uniformly distributed in the interval $[-1, 1]$. The value of the constant c determining the intensity of the noise is equal to 0.05 in the first set of the reconstructions (phantom #1, Figure 7), and to 0.1 in the second set (phantom #2, Figure 8).

Images (a) in Figures 7 and 8 were reconstructed using the present algorithm; Figures 7(b) and 8(b) represent reconstructions computed with projection generation; images (c) were obtained by the multiplicative correction, and, finally, images (d) show results of FBP reconstruction from non-attenuated noisy data. One can notice that the present method (Figures 7 and 8) is more sensitive to the noise than the FBP techniques, and, accordingly, produces more artifacts in the reconstructed image — which is not a surprising result, taking into account that a more ill-posed problem is solved. On the other hand, we see that the technique of multilicative correction (which reduces the problem to the unattenuated case) produces images of the same quality as the ones obtained from unattenuated noisy projections using the FBP algorithm. In other words, combining the Novikov's reconstruction formula with the method of multiplicative correction one obtains a non-iterative SPECT technique that is operative in the case of arbitrary realistic attenuation, and that is as stable as the classical FBP algorithm.

Acknowledgments

After this work had been completed, Professor F. Natterer informed us that he independently implemented a similar algorithm; we express our gratitude to F. Natterer for the information. The author is also indebted to Professor P. Kuchment for encouragement and helpful comments, and to Dr. W. G. Hawkins for numerous discussions.

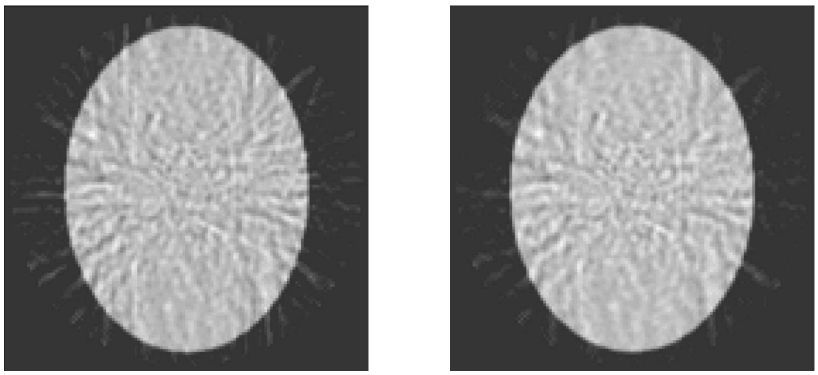

(a)

(b)

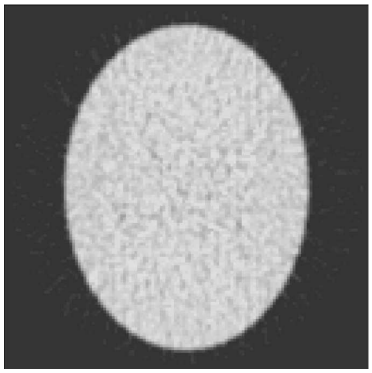

(c)

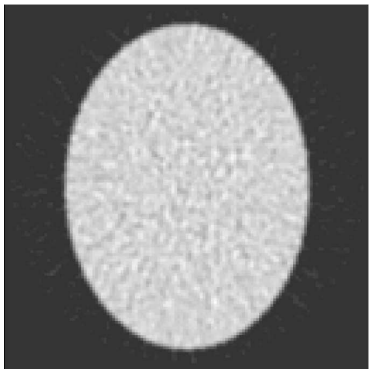

(d)

Figure 7: Reconstruction from noisy data, phantom #1, $c = 0.05$ (a) present algorithm (b) present algorithm with projection generation (c) present algorithm with multiplicative correction (d) FBP reconstruction from non-attenuated noisy measurements.

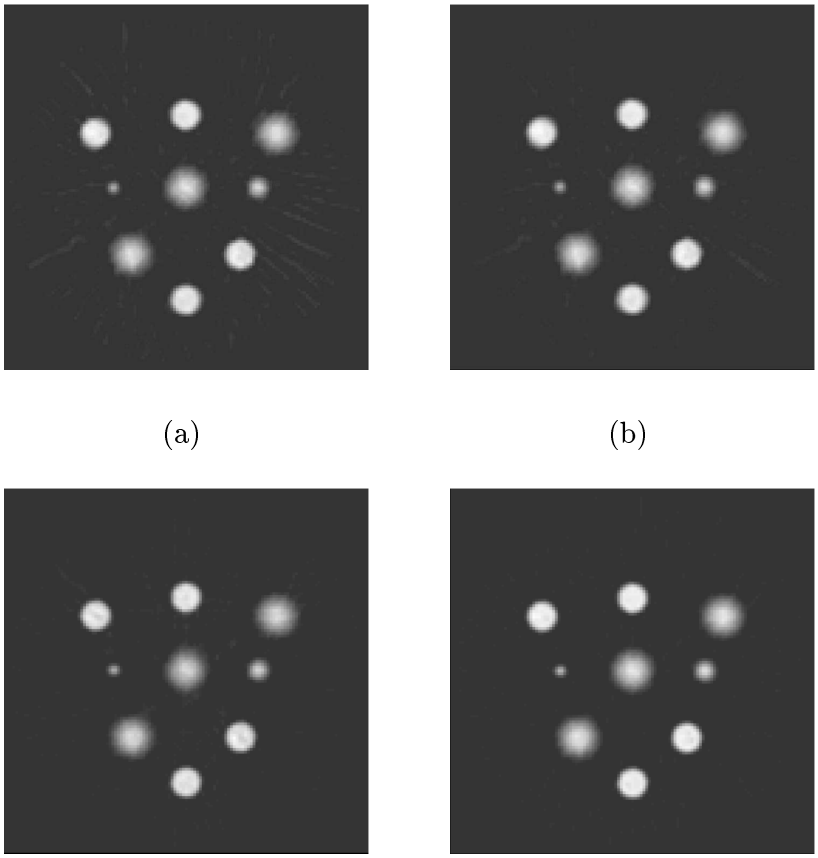

(a) (b)

(c) (d)

Figure 8: Reconstruction from noisy data, phantom #2, $c = 0.1$ (a) present algorithm (b) present algorithm with projection generation (c) present algorithm with multiplicative correction (d) FBP reconstruction from non-attenuated noisy measurements.

References

[1] R. Novikov, *An inversion formula for the attenuated X-ray transformation*, Preprint, May 2000.

[2] F. Natterer, *Inversion of the attenuated Radon transform*, Preprint, August 2000.

[3] S. Bellini, M. Piacentini, C. Cafforio, and F. Rocca, Compensation of tissue absorption in emission tomography, *IEEE Trans. Acoust., Speech, Signal Processing,* ASSP-**27**, (1979), pp. 213-218.

[4] O. J. Tretiak and C. Metz., The exponential Radon transform, *Siam. J. Appl. Math.*, **39** (1980), pp. 341-354.

[5] W. G. Hawkins, P. K. Leichner, and N. C. Yang, The circular harmonic transform for SPECT reconstruction and boundary conditions on the Fourier transform of the sinogram, *IEEE Trans. Med. Imag.,* **7** (1988), pp. 135-148.

[6] T. Inouye, K. Kose, and A. Hasegawa, Image reconstruction algorithm for single-photon-emission computed tomography with uniform attenuation, *Phys. Med. Biol,* **34** (1989), pp. 299-304.

[7] I. Ya. Shneberg, The exponential Radon transform. (Russian) *Dokl. Akad. Nauk SSSR,* **320** (1991), no. 3, pp. 567–571; translation in *Soviet Math. Dokl.* **44** (1992), no. 2, pp. 512–516.

[8] I. Shneiberg, I. Ponomarev, V. Dmitrichenko, and S. Kalashnikov, On a new reconstruction algorithm in emission tomography, in *Applied Aspects of Radon Transform,* S.Gindikin (Ed.), AMS Transl, **162** (1994), pp. 247-255.

[9] C. E. Metz and X. Pan, A unified analysis of exact methods of inverting the 2-D exponential Radon transform, with implications for noise control in SPECT, *IEEE Trans. Med. Imag.,* **14** (1995), pp. 643-658.

[10] P. Kuchment and I. Shneiberg, Some inversion formulas in the Single Photon Emission Tomography, *Applicable Anal.*, **53** (1994), pp. 221-231.

[11] P. Kuchment, On inversion and range characterization of one transform arising in emission tomography, *in Proceedings of the Conference "75 years of the Radon transform"*, Internat. Press 1994, pp. 240-248.

[12] E. V. Arbuzov, A. L. Bukhgeim,. and S. G. Kazantsev, Two-dimensional tomography problems and the theory of A-analytic functions, *Siberian Advances in Mathematics*, **8**, no. 4, (1998), pp. 1-20.

[13] E. Veklerov and J. Llacer, MLE reconstruction of a brain phantom using a Monte-Carlo transition matrix and a statistical stopping rule, *IEEE Trans. Nucl. Sci.*, **NS-35** (1988), no.1, pt. 1, pp. 603-607.

[14] T. Hebert, R. Leahy and M. Singh, Fast MLE for SPECT using an intermediate polar representation and a stopping criterion, *IEEE Trans. Nucl. Sci.*, **NS-35** (1988), no.1, pt. 1, pp. 615-619.

[15] B. M. W. Tsui, H. -B. Hu, D. R. Gilland and G. T. Gullberg, Implementation of simultaneous attenuation and detector response correction in SPECT, *IEEE Trans. Nucl. Sci.,* **NS-35** (1988), no.1, pt. 1, pp. 778-783.

[16] Z. Liang and H. Hart, Bayesian reconstruction in emission computerized tomography, *IEEE Trans. Nucl. Sci.*, **NS-35** (1988), no.1, pt. 1, pp. 788-792.

[17] B. M. W. Tsui, G. T. Gullberg, E. R. Edgerton, J. G. Ballard, J. R. Perry, W. H. McCartney and J. Berg, Correction of nonuniform attenuation in cardiac SPECT imaging, *J. Nucl.Med.*, **30** (1989), pp. 497-507.

[18] G. L. Zeng, G. T. Gulberg, B. M. W. Tsui and J. A. Terry, Three-dimensional iterative reconstruction algorithms with attenuation and geometric point response correction, *IEEE Trans. Nucl. Sci.,* **NS-38** (1991), no. 2, pp. 693-702.

[19] D. S. Lalush and B. M. W. Tsui, Improving the convergence of iterative backprojection algorithms, *Med. Phys.*, **21** (1994), no. 8, pp. 1283-1286.

[20] F. Natterer, *The mathematics of computerized tomography,* John Wiley & Sons, New York, 1986.

[21] L. T. Chang, A method for attenuation correction in radionuclide computed tomography, *IEEE Trans. Nucl. Science,* **NS-25** (1978), pp. 638-643.

[22] S. H. Manglos, R. I. Jaszczak, C. E. Floyd, L. J. Hahn, K. L. Greer, and R. E. Coleman, Nonisotropic attenuation in SPECT: Phantom tests of quantitative effects and compensation techniques, *J. Nucl. Med*, **28** (1987), pp.1584-1591.

[23] T. Morozumi, M. Nakajima, K. Ogawa and S. Yuta, Attenuation correction methods using the information of attenuation distribution for single photon emission CT, *Med. Imag. Tech.*, **2** (1984), pp. 20-29.

[24] L. A. Kunyansky, Generalized and attenuated Radon transforms: restorative approach to the numerical inversion, *Inverse Problems,* **8** (1992), pp. 809-819.

[25] S. C. Blankespoor, X. Wu, K. Kalki, J. K. Brown, H. R. Tany, C. E. Cann, and B. H. Hasegawa, Attenuation correction of SPECT using X-ray CT on an emission transmission CT system: Myocardial perfusion assesment, *IEEE Trans. Nucl. Sci.*, **NS-43**, no. 4, (1996), pp. 2263-2274.

[26] S. Kimiaei and S. A. Larson, Simultaneous SPECT and CT with an opposed dual head gamma camera system and a conventional parallel hole collimators, *IEEE Trans. Nucl. Sci.*, **NS-43,** no. 4, (1996), pp. 2239-2243.

[27] G. A. Korn and T. M. Korn, *Mathematical handbook for scientists and engineers; definitions, theorems, and formulas for reference and review,* McGraw-Hill, New York, 1961

[28] I. S. Gradshtein and I. M. Ryzhik, *Table of Integrals, Series, and Products*, Academic Press, New York, 1980.

[29] M. Abramowitz and I. A. Stegun, *Handbook of Mathematical Functions*, Dover Publications, New York, 1972.

Appendix

In this Appendix we show that the Hilbert transform $HA_\varphi(p)$ of the function $A_\varphi(p)$ given by Equation (18) is equal to μp for $|p| < 1$. Thus, we have to evaluate the following integral (understood in the Principal Value sense);

$$\begin{aligned} HA_\varphi(p) &= \frac{1}{\pi}\mathcal{P}\int_{-1}^{1}\frac{\mu\sqrt{1-v^2}}{p-v}dv \\ &= \frac{\mu}{\pi}\lim_{\varepsilon\to 0}[F_p(p-\varepsilon) - F_p(-1) + F_p(1) - F_p(p+\varepsilon)], \end{aligned} \tag{24}$$

where the primitive $F_p(v)$ satisfies the equation

$$\frac{d}{dv}F_p(v) = \frac{\sqrt{1-v^2}}{p-v}.$$

The explicit expression for $F_p(v)$ can be derived by using formulas 2.261, 2.266, 2.267 of [28], and by taking into account the relation between the inverse hyperbolic tangent and cotangent 4.6.7 of [29]:

$$\begin{aligned} F_p(v) &= -\sqrt{1-v^2} + p\arcsin v + \frac{1}{\sqrt{1-p^2}}\operatorname{arccoth} u(p,v), \\ u(p,v) &= \frac{1-pv}{\sqrt{1-p^2}\sqrt{1-v^2}}, \quad |p|<1. \end{aligned} \tag{25}$$

Substituting (25) into Equation (24) we obtain

$$\begin{aligned} HA_\varphi(p) &= \frac{\mu}{\pi}\left[\pi p + \frac{1}{\sqrt{1-p^2}}\lim_{\varepsilon\to 0}(\operatorname{arccoth} u(p,p-\varepsilon) - \operatorname{arccoth} u(p,p+\varepsilon))\right] \\ &= \mu p + \frac{\mu}{\sqrt{1-p^2}}\lim_{\varepsilon\to 0}(\operatorname{arccoth} u(p,p-\varepsilon) - \operatorname{arccoth} u(p,p+\varepsilon)). \end{aligned} \tag{26}$$

Notice that the function $u(p,v)$ is at least twice differentiable on the open unit square $]-1,1[\times]-1,1[$; for a fixed p function $u(p,v)$ achieves at the point $v=p$. Therefore, in a small neighborhood of p $u(p,v)$ admits the following expansion

$$u(p,p+\varepsilon) = 1 + \frac{1}{2}\frac{\partial^2}{\partial v^2}u(p,p)\varepsilon^2 + \mathcal{O}(\varepsilon^3).$$

Combining the above expansion with the equivalent representation for the hyperbolic cotangent

$$\operatorname{arccoth} x = \frac{1}{2}\ln\frac{x+1}{x-1}$$

one can show that the limit in (26) is equal to zero, which yields the desired result

$$HA_\varphi(p) = \mu p, \quad |p|<1.$$